Aerodynamic Control of Micro Air Vehicle Wings Using Electroactive Membranes

Michael R. Hays [1], Jeffrey Morton [2], Benjamin Dickinson [3], Uttam K. Chakravarty[4], William S. Oates [5]

Florida Center for Advanced Aero Propulsion (FCAAP)[1,2,5]

Department of Mechanical Engineering

Florida A & M and Florida State University

Tallahassee, FL 32310

Munitions Directorate, Air Force Research Laboratory[3,4],

Eglin AFB, FL 32542

Abstract

Dielectric elastomer materials are ideal candidates for developing high agility micro-air-vehicles (MAV) due to their electric field induced deformation. Consequently, the aero-structural response and control authority of the dielectric elastomer material, VHB 4910, is characterized on an elliptical membrane wing. An experimental membrane-wing platform was constructed by stretching VHB 4910 over a rigid elliptical wing-frame. The low Reynolds number (chord Reynolds number $< 10^6$) aerodynamics of the elliptical wing were characterized when different electrostatic fields were applied to the membrane. We observe an overall increase in lift with maximum gains of 20% at an applied voltage of 4.5 kV and demonstrate the ability to delay stall. The time-averaged aerodynamic surface pressure is also investigated by comparing sting balance data and membrane deformation measured using visual image correlation (VIC). The experimental results are compared to a nonlinear finite element membrane model to further understand the effects of aerodynamic load and electric fields on membrane displacements. Model predictions

[1]Email: mrh04c@fsu.edu, Telephone: (850)410-6172

[2]Email: jtm06@fsu.edu, Telephone: (850)410-6172

[3]Email: benjamin.dickinson.1@us.af.mil, Telephone: (850)883-2645

[4]Email: uttamk@gatech.edu, Telephone: (850) 833-9355

[5]Email: woates@eng.fsu.edu, Telephone: (850) 410-6190

of surface pressure provide insight into how the electrostrictive constitutive relations influence the fluid-structure interactions of the membrane. This is validated by comparing lift predictions from the model with time-averaged wind tunnel lift measurements near stall.

1 Introduction

Smart materials are known for their multi-functional material characteristics which are ideal candidates for developing small scale, complex systems and structures that can rapidly adapt to changes in environmental conditions. These materials are promising for developing next generation micro air vehicles that can change their flight characteristics by integrating the adaptive materials directly into the structure of the wings. The most well known types of smart materials include ferroelectric ceramics, Jaffe et al. (1971); Lines and Glass (1977), magnetostrictive compounds, Bertotti (1998); Kittel (1949), and shape memory alloys, Boyd and Lagoudas (1996); Huang and Brinson (1998). These materials often require large power supplies or magnetic coils to convert electric or magnetic fields or heat into mechanical work. In contrast, active polymers have begun to emerge as viable artificial muscles, Bar-Cohen and Zhang (2008). These materials include dielectric elastomers (Kofod and Sommer-Larsen, 2005), shape memory polymers (Liu et al., 2006), ionic polymers and a relatively broad class of nanocomposites (Baur and Silverman, 2007), and liquid crystal polymer networks (Warner and Terentjev, 2007).

In this analysis, the dielectric elastomer VHB is chosen as the adaptive wing material due to its large shape change from an applied electric field and its low stiffness that allows it to more easily conform to the external flow. These materials are known to undergo on the order of 100% field induced deformation which makes them promising materials for developing adaptive small scale aircraft wings (Kofod and Sommer-Larsen, 2005). Deformation is induced by unlike charges that accumulate on opposing sides of the film via a soft electrode material. These unlike charges attract each other forcing the film into compression in the thickness

direction. This subsequently leads to in-plane expansion. In the case of an aerodynamic load on a stretched dielectric elastomer membrane wing, the transverse pressure load results in changes in wing camber as the applied electric field changes. The fields used in the experiments are typically on the order of 10-100 MV/m.

Whereas significant fundamental theoretical and experimental mechanics research has focused on the electromechanics of dielectric elastomers, Bustamante et al. (2009); Fox and Goulbourne (2009); McMeeking and Landis (2005); Plante and Dubowsky (2006); Wissler and Mazza (2005); Zhao et al. (2007), no research to the authors' knowledge has focused on quantifying the aerodynamic effect of these materials on lift surfaces in the low Reynolds number regimes of MAV flight (chord Reynolds number $< 10^6$). In comparison, recent analytical, computational, and experimental studies of passive membranes have been studied; see Gordnier (2009); Molki and Breuer (2010); Rojratsirikul et al. (2010); Song et al. (2008) for examples. Soft dielectric elastomer materials are typically stretched over a rigid outer ring structure to increase deformation and reduce reliability from premature dielectric breakdown. Such structures are ideal for stretching over a rigid MAV wing structure to study electric field controlled shape changes in response to low Reynolds number aerodynamic loads. These concepts are explored here experimentally in low Reynolds number wind tunnel tests and compared to a model of a finite deforming, hyperelastic membrane to understand deformation induced by aerodynamic loads versus relaxation from electrostatic stresses.

It is shown that the dielectric elastomer, VHB 4910, is capable of substantial aerodynamic influence, including increasing lift and mitigating stall. Our experimental platform is composed of a dielectric elastomer film that is pre-stretched approximately 300% and adhered to a rigid elliptical wing-frame. A uniform field is applied through the thickness of the membrane using a compact, high voltage amplifier and carbon grease as the electrode material. The aerodynamic behavior is quantified at different angles of attack for chord Reynolds numbers, Re_c, of 38k and 63k using a six degree of freedom sting balance and stereographic imaging using two high speed cameras (1000 fps). The results illustrate a 20% increase in lift at Re_c=63k when the voltage is increased to 4.5 kV relative to the 0 kV case. Comparable behavior is

measured at Re_c=38k. The high speed camera images also illustrate changes in shape of the membrane under different electric fields and aerodynamic loads.

To better understand the aerodynamic behavior, we compare the wind tunnel data to a finite deformation, electro-mechical finite element membrane model. The modeling framework couples the VIC displacement data directly such that pressure can be calculated as a function of membrane displacements, pre-stretch, hyperelastic constitutive relations, and electrostatic stresses. Once the pressure is calculated over the surface of the membrane, the lift force can be calculated and compared with sting balance data. This approach provides useful information in correlating electro-mechanical constitutive relations with aerodynamic loads. In this initial analysis, we compare time-averaged deformation of the membrane with average lift data measured from the sting balance. It is shown in Section 4 that reasonable predictions of lift are calculated at small to moderate membrane displacements by fitting a hyperelastic constitutive model to uniaxial data and dielectric constants from the literature without any additional fitting parameters associated with the flow environment.

The experimental set-up and results of the analysis are summarized as follows. First, a description of the experimental wind tunnel set-up and elliptical wing structure are given. The experimental results are then presented and compared to a finite deformation membrane model to estimate the pressure on the wing surface as a function of the hyperelastic behavior and different electrostatic fields. Concluding remarks are given in the final section.

2 Experimental Setup

The electroactive MAV wing structure is first described followed by the experimental set-up in the low Reynolds number wind tunnel. The data collected during the experiments included mounting the wing on a six degree of freedom sting balance and a visual image correlation system that allowed for measurement of *in situ*, time-dependent three dimensional deformation of the electroactive wing.

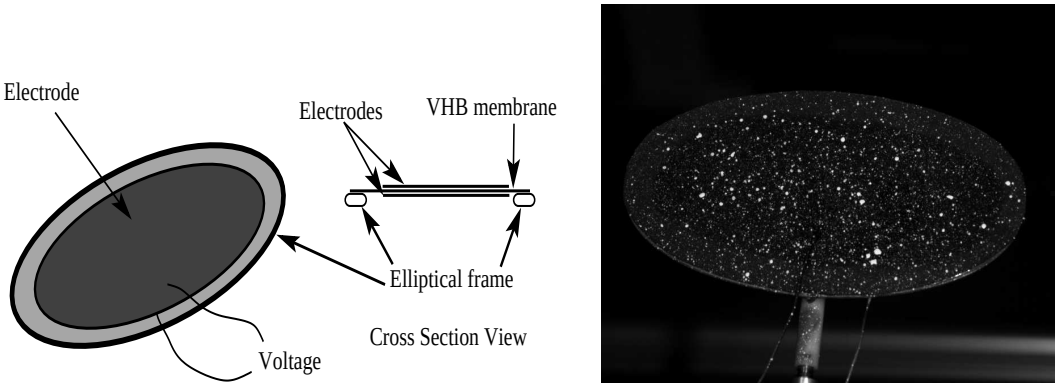

(a) (b)

Figure 1: (a) Electroactive elliptical wing concept. (b) Image of the 20×10 cm^2 electroactive elliptical wing (maximum width and height). A white speckle pattern is applied to quantify time dependent deformation under different electric fields and aerodynamic loads.

2.1 Active Wing Structure

A rigid elliptical wing-frame (major and minor axes of 20 cm and 10 cm, respectively) served as an external structure to hold the electroactive membrane. VHB 4910 was used as the membrane material which was bi-axially pre-stretched to approximately 300% strain and attached to the elliptical structure. A thin layer of carbon grease was applied to the top and bottom of the membrane for applying an electric field through the thickness of the wing. As the field is applied, compressive electrostatic stresses are created from unlike charges on the top and bottom of the membrane which results in in-plane expansion. The electric field was applied using an EMCO C60 compact high voltage linear amplifier that converts 0-5 V into 0-6 kV with a maximum current of 0.166 mA. The wing concept and experimental configuration are illustrated in Figure 1. The speckled pattern shown in Figure 1(b) is used to quantify time-dependent deformation of the membrane during wind tunnel testing. Details describing these measurements are given in the following section.

2.2 Wind Tunnel and Camera Set-Up

Wind tunnel tests were performed in an open circuit, low turbulence, low-Reynolds number wind tunnel located the University of Florida Research and Engineering Education Facility (UF-REEF), Albertani et al. (2009). Wing angle of attack was controlled with a pitch-plunge rig where the main components are a pair of Trilogy ironless magnetic linear motors (Parker Automation) with Aries Servo Drivers (Parker Automation, AR20AE) and controlled by a DMC-2020 model motion controller (Galil Motion Control). For further description of the pitch-plunge rig see, Albertani and Babcock (2008). Wing inclination was measured with a VTI Technologies SCA121T-D03 inclinometer. Aerodynamic force and moment measurements were made with an Allied Aerospace MC-.10-.375 6 channel sting balance with a resolution of 0.1 N. Sting balance measurements were received through a 24-bit strain measurement card (National Instruments, SCXI 1520) and fed to an analog to digital converter (National Instruments, SCXI 1600). Dynamic pressure measurements were made with a pitot tube and Heise ST-2H pressure transducer. Atmospheric pressure was measured with a Druck DPI 142 precision barometric indicator.

The time dependent, three dimensional membrane shape and deformation due to electrical and aerodynamic loads were characterized with VIC. This measurment technique involves tracking the deformation of a random speckle pattern applied to the structure (membrane, see Figure 1b) under loading. Here, white paint was speckled onto the black carbon grease that covered the top surface of the membrane. Two high speed digital cameras recorded the speckle pattern displacement through a sequence of snapshots. Surface displacement and strain data were obtained using the commercial software, VIC3D, by maximizing the normalized cross-correlation between subsequent images.

3 Experimental Results

3.1 Aerodynamic Force Characterization

The three degree-of-freedom aerodynamic data of the electroactive compliant wing is quantified and compared to a rigid elliptical wing. The rigid wing was constructed by adhering 0.02" thickness aluminum to the elliptical perimeter. For each voltage appled to the membrane wing, static wind tunnel tests were performed at flow speeds of 6 m/s and 10 m/s for angles of attack (AOA) ranging from 0 to 26°. Figure 2 contains the results for 6 m/s (chord Reynolds number 38k).

Each data point in Figure 2 is the mean of 20 data sets, where each set is composed of 500 measurements recorded at 500 Hz. The compliant electroactive wing created more lift than the rigid wing, although exceptions were observed for 0 V near 10° and AOA beyond 17°. The effect of the 3.6 kV and 4.5 kV electric potential was an upward shift of the lift curve, characteristic of an increase in camber due to the applied field. Positive lift at 0° AOA was measured for the compliant wing, indicating positive camber. For 0, 3.6, and 4.5 kV, the point of stall was delayed by approximately 2° compared to the rigid wing. However, due to AOA resolution, whether the activated wing delays stall beyond the passive 0 V case is not clear.

Drag force was also affected by passive membrane deformation and the applied electric fields (Figure 2b). Below 10°, drag for the 0, 3.6, and 4.5 kV cases was less than the rigid wing where a marginal increase in drag with respect to voltage is indicated. Above 10°, all compliant cases created more drag than the rigid wing. Given the lift and drag behavior, it follows that compliant wing efficiency (C_L/C_D) is largest below 10° AOA for the 0 V case. The pitching moment also increases as the voltage increases as shown in Figure 2(c). In all pitching moment calculations, the moment is taken about the 1/4 chord position relative to the leading edge. As expected, the pitching moment for the flat plate about this point is approximately zero. Aerodynamic efficiency at higher AoA is increased by the application of an electric field between 10° to 17°. It is also interesting to note that the zero voltage case

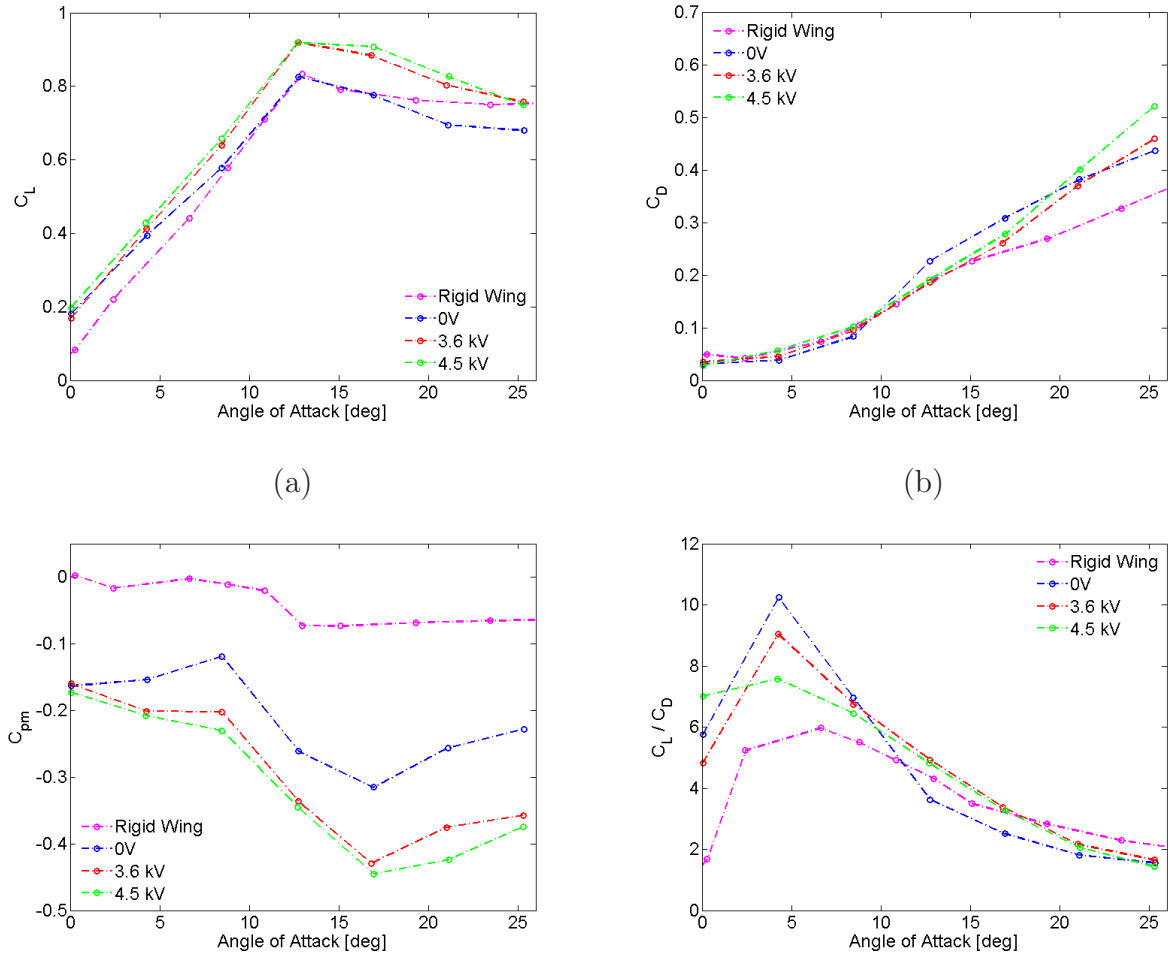

Figure 2: Coefficient of lift (a), drag (b), pitch-moment (c), and lift to drag ratio (d) versus angle of attack. The different lines represent a rigid elliptical wing (solid line, "-") and electroactive elliptical wing at 0 V (dashed line, "- -"), 3.6 kV (dash-dot line,"-.-"), and 4.5 kV (dotted line, "$\cdots$") at a chord Reynolds number of 38.7k.

provided the largest aerodynamic efficiency at a lower AoA near 5°. This suggests the increase in camber and/or the reduction in tension from the applied field increases the drag and reduces the lift of the wing disproportionately to the zero voltage case. It is also important to note that there is higher measurement uncertainty at this speed as the drag forces approach the resolution of the sting balance at AOA$\leq$ 10°.

The aerodynamic force measurements illustrated Figure 2 are similarly observed at a chord

Reynolds number of 63k as shown in Figure 3. The increase in the Reynolds number from 38k to 63k resulted in an upward shift in the lift curve (Figure 3a). Prior to stall, the passive compliance of the membrane wing provided the largest contribution to increased lift while that due to the applied voltage was marginal. Beyond 12.5°, the 4.5 kV case indicates stall is prevented 5° prior to the passive compliant wing (0 V) and 7° prior to the rigid wing. In comparison to the 0 V case, near 17° AOA a 5% and 20% increase in lift occurs for 3.6 kV and 4.5 kV, respectively.

Drag of the electroactive wing is less than the rigid wing from 0 to 13° AOA and up to roughly 30% greater drag beyond 13°. Below 17°, the elecric field activated wing shows less drag than the passively compliant case. The decreased drag and increased lift of the active wing leads to a substantially improved aerodynamic efficiency (C_L/C_D) over the rigid and passive compliant wings. The greatest was efficiency observed at 3.6 kV. This is in contrast to the Re_c=38k scenario (Figure 2d), where the greatest efficiencies were found at 0 V near 5° AOA.

On the basis of the aerodynamic data presented herein, we find that the electroactive membrane wing has significant authority to augment aerodynamic forces acting on the wing. We observe a general increase in lift and find evidence of a significant delay of stall at Re_c=63k, with a potential delay of stall also at Re_c=38k. It is also interesting to note the difference in aerodynamic efficiencies as a function of voltage for the two different Reynolds numbers. The zero voltage tension gave a maximum efficiency at Re_c=38k whereas optimal efficiency at Re_c=63k was achieved with a 3.6 kV applied voltage. Clearly, the optimal aerodynamic efficiency requires different pre-tensions for different Reynolds numbers. In the following section we explore wing strain and displacement fields at 17° AOA, where the largest changes in lift due to the dielectric elastomer were observed.

3.2 Structural Deformation Characterization

In this section, the membrane wing deformation measurements for different applied voltages and Reynolds numbers (38k and 63k) are given for an AOA of 17°. As illustrated in

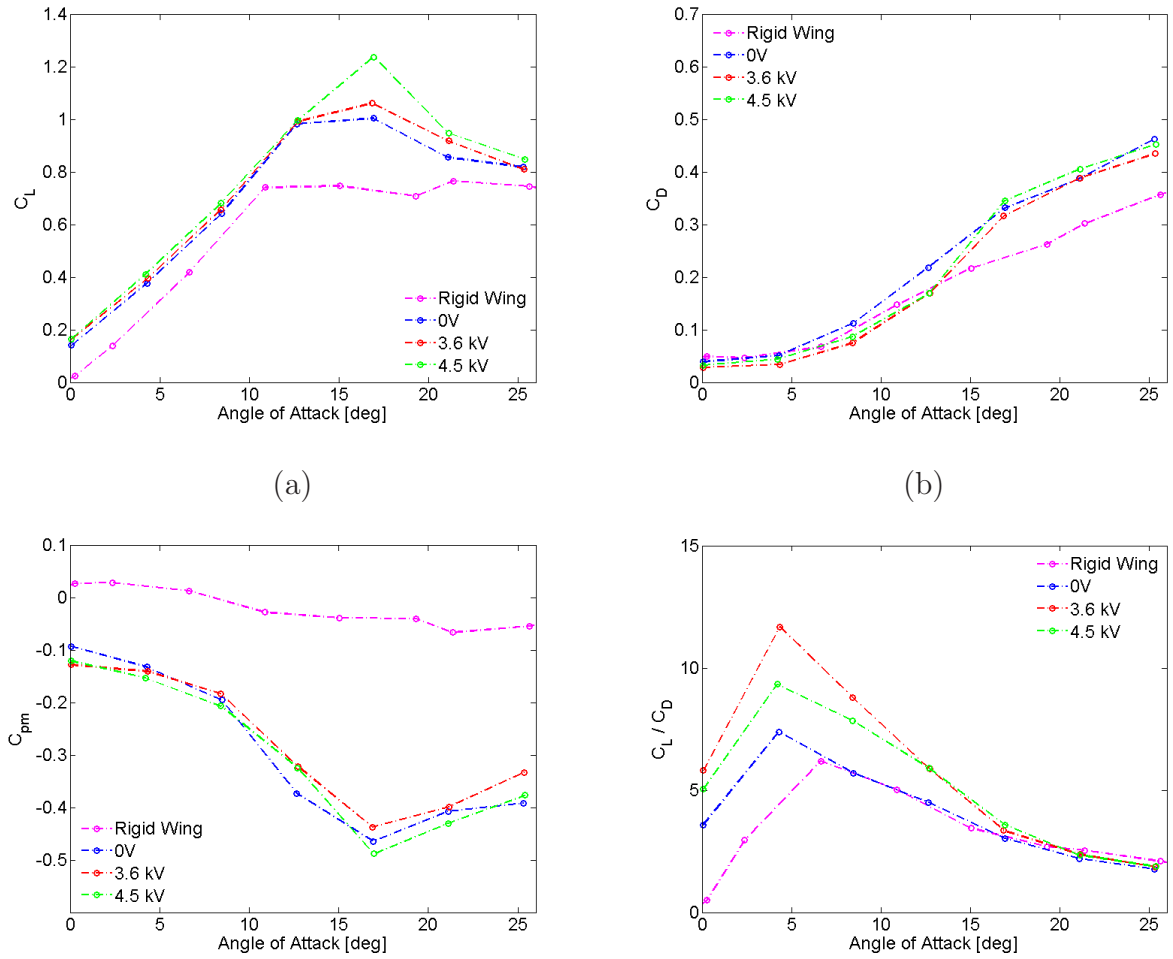

Figure 3: Coefficient of lift (a), drag (b), pitch-moment (c), and lift to drag ratio (d) versus angle of attack. The different lines represent a rigid elliptical wing (solid line, "-") and electroactive elliptical wing at 0 V (dashed line, "- -"), 3.6 kV (dash-dot line,"-.-"), and 4.5 kV (dotted line, "$\cdots$") at a chord Reynolds number of 63k.

Figure 1, the effect of the applied voltage creates an attractive force between the electrodes. This creates compression of the VHB material in the thickness direction and lateral expansion in the plane of the membrane. In the wing structure, the electrodes do not completely extend to the outer region of the elliptical frame since this frame is metallic and may result in electric arcing. Thus, inhomogeneous strain is observed in this outer elliptical band near the frame.

The changes in strain under an aerodynamic load for the electrostatic voltages, 3.6 kV

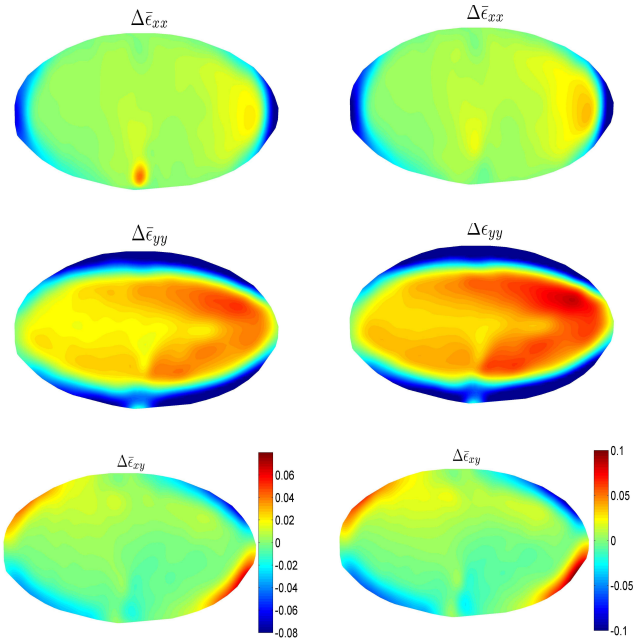

Figure 4: The change of in-plane electrically induced strain $\Delta\bar{\epsilon}_{xx}$ (*top*), $\Delta\bar{\epsilon}_{yy}$ (*middle*), and $\Delta\bar{\epsilon}_{xy}$ (*bottom*) due to 3.6 kV (*left*) and 4.5 kV (*right*) for Re = 38k. The colorbars represent strain on the bottom row apply column-wise and ± 6% for 3.6 kV and ± 10% for 4.5 kV.

and 4.5 kV, are illustrated in Figures 4 and 5. In these figures, the mean change in strain fields $\Delta\bar{\epsilon}_{xx}$, $\Delta\bar{\epsilon}_{yy}$, and $\Delta\bar{\epsilon}_{xy}$ are plotted for both Re_c=38k and 63k. The average strain fields at 0 kV are not included for brevity. These strain fields were approximately an order of magnitude lower that the strain fields under the applied electric fields. The average strain field were computed from 500 snapshots taken at 17° AOA at 1 kHz for the chord Reynolds numbers and voltages presented in Section 3.1; however, for Re_c=38k and 3.6kV, only 277 snapshots were available. The snapshot rate and duration were chosen to resolve several periods of oscillations observed in the wing membrane. Throughout this paper, the leading edge is oriented at the top of the elliptical images.

As noted above, zero voltage aerodynamic loads create relatively small strains relative to the case when an electric field is present so that Figure 4 effectively illustrates the combined effect of the electric field and fluid-structure interactions at Re_c=38k. We note that non-uniform changes in strain are apparent on the right side of $\Delta\bar{\epsilon}_{xx}$ and $\Delta\bar{\epsilon}_{yy}$ fields which may be caused by non-uniformities in VHB pre-tension or VHB thickness. Regardless of this

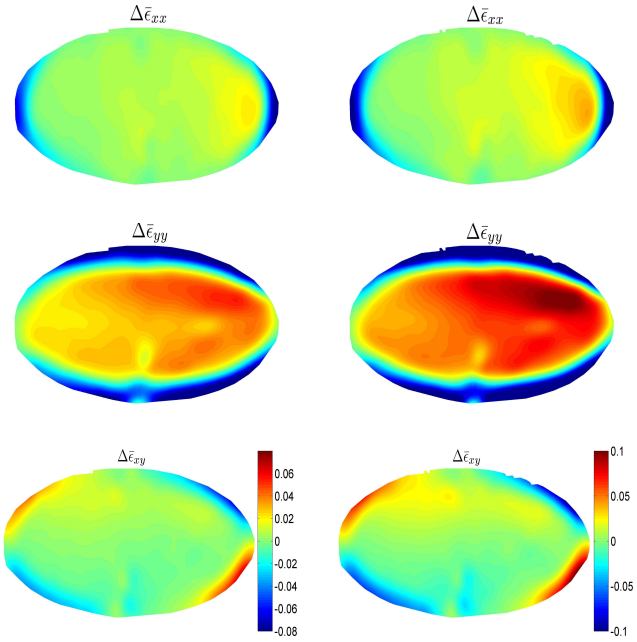

Figure 5: Mean change in plane strain $\Delta\bar{\epsilon}_{xx}$ (*top*), $\Delta\bar{\epsilon}_{yy}$ (*middle*), and $\Delta\bar{\epsilon}_{xy}$ (*bottom*) due to 3.6 kV (*left*) and 4.5 kV (*right*) for Re = 63k. The colors bars representing strain on the bottom row apply column-wise with ± 6% for 3.6 kV and ± 10% for 4.5 kV.

variation in strain, the effect of the aerodynamic load on strain is significant for Re_c=63k versus Re_c=38k as illustrated by comparing Figure 4 to Figure 5.

Significant unsteadiness was observed in the membrane shape response for the Reynolds numbers considered. The variance of the change in strain fields $\Delta\bar{\epsilon}_{xx}$, $\Delta\bar{\epsilon}_{yy}$, and $\Delta\bar{\epsilon}_{xy}$ under aerodynamic loading was small relative to the strain state as quantified in Table 1. Increasing the chord Reynolds number increased the standard deviation of the fluctuations in strain state. However, these fluctuations are small compared to the magnitude of the change in strain from the applied electric fields.

Under an aerodynamic load, we find that the overall structural effect of the applied voltage is relaxation, as indicated by an increase in out-of-plane displacement of the wing membrane as shown in Figure 6. Time resolved movies of out-of-plane displacement show membrane oscillation around a state of positive camber. Standard deviations of displacement data (Figure 7), show that the displacement fluctuations increase with Reynolds number and voltage, although they are small compared to the magnitudes of the respective mean displacements.

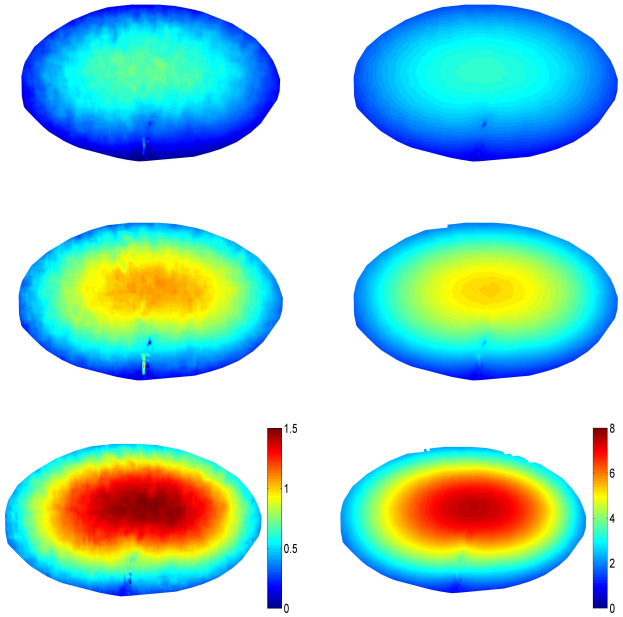

Figure 6: Mean out-of-plane displacement (millimeters) at 17° AOA, Re_c=38k (*left*) and Re_c=63k (*right*) for 0 V (*top*), 3.6 kV (*middle*), and 4.5 kV (*bottom*), color scales for each Reynolds number are assigned column-wise and indicated by color bars on the bottom row

For all voltages at Re_c=38k and the 0 kV at Re_c=63k case in Figure 7, the standard deviation fields are less smooth (grainy appearance) than the 3.6 kV and 4.5 kV cases at Re_c=63k. This result may be due to the accuracy limitations of the VIC measurements.

In summary, the applied electric field to the VHB material provides a means for effective reduction of the initial pre-tension in the membrane wing. In turn, this allows for active control of wing camber through coupling between aerodynamic loading and changes in the effective wing membrane tension as a function of the applied field. In the following section, we apply a nonlinear membrane finite element model to compare the effect of aerodynamic load and electrostatic stresses for the Re_c=63k case at an AOA of 17°. This corresponds to the point near stall that was illustrated in Figure 3(a).

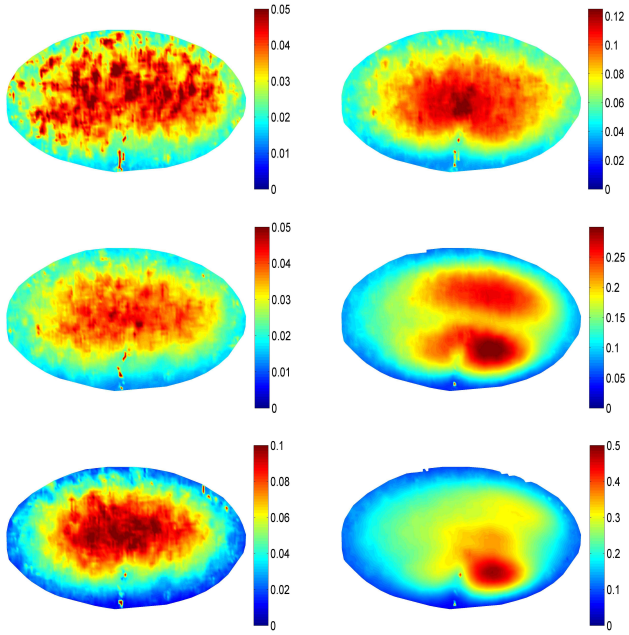

Figure 7: Standard deviation of out-of-plane displacement (millimeter) at 17° AOA, Re=38k (*left*) and Re=63k (*right*) for 0 V (*top*), 3.6 kV (*middle*) and 4.5 kV (*bottom*)

4 Model Comparisons

A nonlinear membrane model is numerically implemented and used for comparisons to the experiments to further understand the fluid-structure interactions. The governing equations are first summarized and then implemented in a commercial finite element software package, Comsol 4.2. The VIC displacement data is coupled to the model such that the finite element nodal displacements are constrained to closely match the experimental VIC data. This approach is used to reduce uncertainty in calculating the surface pressure induced by the unsteady three-dimensional flow field. Whereas several fluid-structure computational methods exist to calculate the fully-coupled behavior when the wing is immersed in a fluid (Bin et al. (2011); Cottet et al. (2008); Dunne and Rannacher (2006); Gordnier (2009); **?**), three dimensional computational methods become prohibitively expensive. The aerodynamic pressure may also be calculated from the displacement if the membrane tension is known by calculating the membrane curvature. This can be achieved if the curvature can be accurately calculated from displacements. This approach typically requires small displacements, rotations, and con-

stant tension. Here, we focus on application of the finite deformation membrane model and coupling with displacement data to determine the aerodynamic pressure under different electrostatic fields. This approach provides information about the tension through the use of an electrically-coupled hyperelastic constitutive model and is not limited to small displacements and rotations.

The membrane equations for the finite deformation case are numerically implemented to calculate tension after a bi-axial pre-stretch of $\lambda_0 = 3$, applied electric fields and aerodynamic pressure loads. The governing equations are given in terms of the variation of the internal energy which include a minimization of mechanical energy combined with a penalty method that constrains the finite element nodal displacements to the VIC displacement data. Electrostatic energy is treated separately since the field in the reference configuration is uniform across the majority of the membrane and therefore can be calculated explicitly. This field is inserted into an electromechanical stress relation. Note that this approximates the edge conditions as these regions do not contain electrodes as illustrated in Figure 1.

The variation of the mechanical energy is

$$\delta W_M = H \int_{\Omega_0} \widetilde{T}_{IJ} \delta E_{IJ} dA_0 - \int_{\Omega_0} e_{pij} \frac{\partial x_i}{\partial X_1} \frac{\partial x_j}{\partial X_2} \Delta p_s \delta u_p dA_0 \tag{1}$$

where only quasi-static deformation is considered. The initial membrane thickness in the unstretched state is denoted by H. The first integral is defined by the product of the second Piola-Kirchhoff stress ($\widetilde{T}_{IJ}$) times the variation of the Green finite deformation strain (δE_{IJ}) integrated over the area of the membrane (Ω_0). The second integral defines coupling to an unknown pressure difference Δp_s across the top and bottom surfaces of the membrane at every point on the membrane surface. The additional terms in the second integral constrain the unknown pressure difference to be normal to the surface using the curl of the deformation gradient components: $\dfrac{\partial x_i}{\partial X_1}$ and $\dfrac{\partial x_j}{\partial X_2}$ where x_i is the deformed material point, X_I is the reference point, and e_{pij} is the permutation symbol. Lastly, the variation in the finite element displacements are δu_p where $p = 1, 2$, and 3. More details on these membrane governing equations are given by Holzapfel (2000); Schweizerhof and Ramm (1984). This equation must

be satisfied over the area Ω_0 subjected to a set of boundary conditions on the perimeter of the membrane. Displacement boundary conditions are used in the model and described in further detail in Section 4.1.

The unknown pressure difference across the membrane thickness is determined using an equation that penalizes differences between the finite element nodal displacements and the VIC displacement measurements. For the transverse loading direction we use

$$\int_{\Omega_0} \left[-a_0 \left(\frac{\partial \Delta p_s}{\partial X_1} \frac{\partial \delta \Delta p_s}{\partial X_1} + \frac{\partial \Delta p_s}{\partial X_2} \frac{\partial \delta \Delta p_s}{\partial X_2} \right) + \beta \left(u_3 - u_3^{VIC} \right) \delta \Delta p_s \right] dA_0 = 0 \tag{2}$$

where the test function for the unknown pressure is denoted by $\delta \Delta p_s$. The first term in parenthesis is a diffusion term that is used to smooth the solution. The parameter a_0 is limited to small values such that artificial diffusion effects on the pressure solution are minimal. This is validated by comparing the error between the finite element nodal displacements and the VIC displacements. The second term contains a positive scalar parameter β that is increased to minimize errors between the transverse displacement data (u_3^{VIC}) and the finite element nodal displacements. The time-averaged in-plane displacements were not constrained to the VIC data since they were two orders of magnitude smaller than the out-of-plane displacements. However note that the pressure solution will influence in-plane displacements through coupling with the deformation gradient in (1). The pressure is unknown on the boundary of the membrane wing; therefore, we approximate the boundary conditions to have a zero pressure gradient on an elliptical boundary that is slightly larger than the physical domain of interest so that it does not influence the internal pressure along the wing dimensions measured using the VIC system. This is discussed in further detail in Section 4.1.

In general, Gauss's law must also be solved to determine the charge displacement for a given electric potential. This can be described in terms of the variation of electrical energy

$$\delta W_E = H \int_{\Omega_0} \widetilde{E}_I \delta \widetilde{D}_I dA_0 - H \int_{\Omega_0} \Phi \delta Q dA_0 \tag{3}$$

where the electric field and variation of electric displacement are denoted by $\widetilde{E}_I$ and $\delta \widetilde{D}_I$, respectively. Both of these variables are given in the reference frame as denoted by $\widetilde{(\cdot)}$. The

electric potential and variation of charge density are denoted by Φ and δQ, respectively. For more details on the electrical governing equations, see Zhao et al. (2007). In the finite element model, the applied field in the reference configuration is uniform and therefore this equation is not solved explicitly. Alternatively, the electric field is applied and inserted into an electrostatic stress constitutive relation as described in the following paragraphs.

The second Piola-Kirchhoff stress in (1) contains stress induced by "mechanically" stretching the membrane and from applying an electric field. The "mechanical" stresses are determined from an Ogden incompressible hyperelastic free energy (Holzapfel, 2000) while the electrostatic stresses are determined from a linear dielectric energy function. These energy functions and the associated stress relations are given as follows.

Following Zhao et al. (2007), we assume the dielectric energy in the elastomer is linear and inversely proportional to the dielectric permittivity, κ. This dielectric energy in the reference configuration is

$$W_E = \frac{F_{iK}F_{iL}}{2J\kappa}\widetilde{D}_K\widetilde{D}_L \tag{4}$$

where F_{iK} is the deformation gradient and $J = \det(F_{iK})$. Since the material may undergo finite deformation, the true electric displacement and electric field in the currently deformed domain are related to the nominal field and nominal electric displacement in the undeformed configuration using the rotationally invariant spatial fields

$$\begin{aligned} D_i &= J^{-1}F_{iK}\widetilde{D}_K \\ E_i &= H_{iK}\widetilde{E}_K \end{aligned} \tag{5}$$

where H_{iK} is the inverse deformation gradient with $F_{iK}H_{jK} = \delta_{ij}$ and δ_{ij} is the Kronecker delta. In the finite element model, the membrane lies in the (X_1, X_2) plane and the field is applied in the X_3 direction, i.e., $\widetilde{\mathbf{E}} = \widetilde{E}_3\hat{N}_3$ where $\hat{N}_3$ is the unit vector normal to the (X_1, X_2) plane.

The constitutive relation between the true electric displacement and true electric field can then be determined from the dielectric energy as

$$D_i = \kappa E_i \tag{6}$$

which assumes the dielectric permittivity is independent of the deformation gradient.

The coupling between the deformation gradient and the electric quantities in (5) results in a total stress that includes components from mechanically stretching the polymer and electrostatic stresses from the applied electric field. The total second Piola-Kirchoff stress is

$$\widetilde{T}_{IJ} = \frac{\partial W_M}{\partial I_1}\delta_{IJ} + JH_{kI}H_{lJ}\sigma^E_{kl} \tag{7}$$

where the mechanical energy (W_M) is written as a function of the first strain invariant, $I_1 = \lambda_i\lambda_i$ where λ_i is the stretch ratio (Holzapfel, 2000). The last term includes the electrostatic Cauchy stress that is defined in terms of the electric field as

$$\sigma^E_{si} = \kappa\left(E_sE_i - \frac{1}{2}E_kE_k\delta_{si}\right) \tag{8}$$

where details on this stress are given by McMeeking and Landis (2005); Zhao et al. (2007).

The mechanical energy density is described by an incompressible hyperelastic Ogden function

$$W_M = \sum_{p=1}^{3}\frac{\mu_p}{\alpha_p}\left(I_1^{\alpha_p} - 3^{\alpha_p}\right) - p(J-1) \tag{9}$$

where μ_p are shear moduli and α_p are unitless constants. The second term constrains the model to be incompressible using the Jacobian J and an undetermined hydrostatic pressure p within the elastomer.

These constitutive relations are introduced into the electrostatic membrane equations (1) and (2) and are solved numerically for a given set of boundary conditions described in Section 4.1.

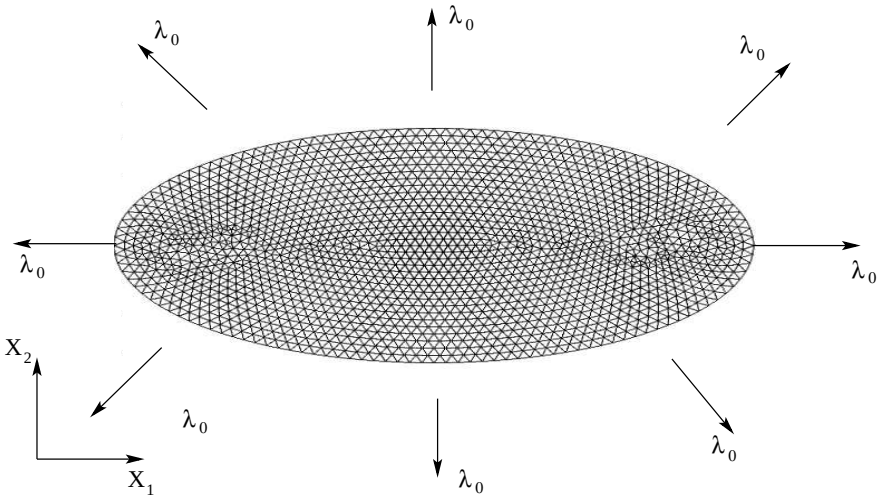

Figure 8: Finite element geometry and mesh. The finite element boundary is defined as an elliptical region slightly larger than the VIC elliptical domain, $[198/\lambda_0,\ 99/\lambda_0]$ in millimeters. Once the membrane is pre-stretched to $\lambda_0 = 3$, an electric field is applied to the entire model followed by constraining the displacement to the VIC data.

4.1 Numerical Implementation

The membrane wing is modeled using an elliptical region that was slightly larger than the region measured by the VIC system. This region is used to approximate the unknown pressure near the boundary. Based on (2), we set the pressure gradient to be zero on the computational boundary and focus on correlation of the internal pressure of the wing area that was measured by the VIC system.

The finite element reference state is defined as the unstretched state and has a major and minor axis of $198/\lambda_0$ mm and $99/\lambda_0$ mm, respectively. The model is given in the reference domain and is therefore scaled by the pre-stretch, $\lambda_0 = 3$. Recall that the VIC data was taken on a elliptical domain that was also smaller than the true wing dimensions. The VIC measurement region was an ellipse with a major and minor axis of $190.8/\lambda_0$ mm and $92.4/\lambda_0$ mm, respectively. The finite element model and boundary conditions are illustrated in Figure 8.

Three sets of quasi-static loads were sequentially applied to the model. First, the model is pre-stretched bi-axially to $\lambda_0 = 3$ to match the deformed geometry of the wing that was

measured with the VIC system during wind tunnel tests. Second, voltages ranging from 0, 3.6, and 4.5 kV were applied to the model by calculating the nominal field for the 1 mm thick membrane. Lastly, the VIC displacements defined in (2) were linearly incremented from zero to the time-averaged values. This was confirmed experimentally based on the VIC data. To facilitate numerical implementation, the displacement data is fit to a polynomial using the Matlab function `fit` and was then inserted into Comsol; see the Appendix. The polynomial fits had R^2 values of 0.994, 0.996, and 0.997 for the 0, 3.6, and 4.5 kV cases, respectively.

To implement the finite element solution, a set of hyperelastic coefficients and dielectric permittivity was identified based on stress-stretch experiments and comparisons to dielectric measurements given in the literature. The hyperelastic coefficients were fit to uniaxial experiments that are described elsewhere (Newton et al., 2012). Figure 9(a) illustrates the comparison between a uniaxial load experiment on VHB 4910 that was conducted at a stretch rate of 3.39×10^{-4} s^{-1} and the hyperelastic model given by (9). We chose a relatively small stretch rate to minimize the effect of viscoelasticity. The model parameters were fit using the Nelder-Mead optimization algorithm in Matlab: `fminsearch`. The material parameters are tabulated in Table 2. In Figure 9(b), predictions of bi-axial stress in terms of the nominmal stress and second Piola-Kirchhoff stress are shown. These stresses provide a measure of the tension experienced by the membrane prior to application of an electric field and aerodynamic load. The dielectric permittivity used in the model was guided by experiments given in the literature (Kofod et al., 2003; Wissler and Mazza, 2007). Wissler and Mazza (2007) measured a relative dielectric permittivity between 3.71 and 3.34 for a pre-stretch of 300% and 400%, respectively. Larger values have been reported to range between 4.5 to 4.7 as a function of pre-stretch (Kofod et al., 2003). It will be shown that values on the lower end of this range were necessary to match wind tunnel lift measurements.

Comparisons between the wind tunnel time-averaged lift data and the finite element model were first compared by analyzing membrane deformation at zero volts followed by model fits at the two applied voltages. The displacements for each voltage are illustrated in Figures 10(a-c) over the entire wing and a direct comparison of each voltage is shown in Figure 10(d) by

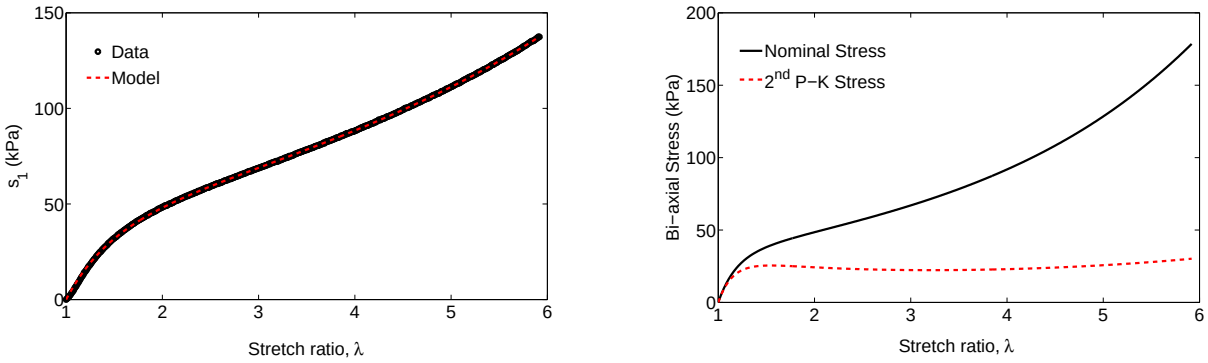

(a) (b)

Figure 9: (a) A comparison of the uniaxial load experiments on VHB 4910 given in (Newton et al., 2012) to a uniaxial model fit of the nominal stress. (b) The corresponding bi-axial stress-stretch relation in terms of the nominal stress and second Piola-Kirchhoff stress.

plotting the displacement along the centerline of the wing chord. In plots (a-c), the air flow is from top to bottom and in (d) the air flow is from right to left. The maximum error between the finite element displacements and the polynomial VIC data fit was 0.32%, 0.063%, and 1.0% for 0 kV, 3.6 kV, and 4.5 kV; respectively. Recall that the displacement solutions are based on penalizing the error between the VIC transverse displacement data and the finite element nodal displacements according to (2). This allows the time-averaged aerodynamic pressure to be determined.

The pressure that is calculated by minimizing the error between the transverse displacement solutions and VIC data is shown in Figure 11 for each voltage tested. Similarly to the displacement solutions, the pressure over the entire wing is shown in Figure 11(a-c) and a direct comparison of each voltage is shown in Figure 11(d) by plotting the displacement along the centerline of the wing chord. The pressure solutions are only given over the VIC measurement domain $[190.8/\lambda_0, 92.4/\lambda_0]$. Spanwise asymmetry in the spanwise direction is shown in these figures which is believed to be due to the uncertainty in uniform pre-stretch of the membrane. The pressure calculated at zero volts is dependent on the hyperelastic coefficients and independent of the dielectric constant. We compare the lift force data with the model by integrating the pressure over VIC measurement domain. Recall that this domain is slightly

smaller than the finite element elliptical domain and true wing geometry. We therefore scale the pressure based on the ratio of the VIC measurement elliptical domain and the true area of the experimental wing geometry. For the case of zero volts, the lift predicted by the finite element model was 0.79 N while the experimental time-averaged lift force was 0.84 N resulting in an error of 6%.

The additional comparisons between pressure calculations and sting lift data was done for the non-zero voltage cases by again integrating the finite element pressure solutions over the wing area. Unlike in the zero voltage case, the dielectric permittivity coefficient influences the lift indirectly since pressure is proportional to membrane tension. This tension is reduced by the electric fields, and subsequently the electrostatic stresses. To achieve a close fit to the lift data, we found that the relative dielectric permittivity must vary between 3.3 and 2.8 as the field is increased from 3.6 kV to 4.5 kV, respectively. This fit gave an exact match to the time-averaged lift force of 0.88 N and 1.09 N for the 3.6 kV and 4.5 kV cases, respectively. Recalling permittivity measurements given in the literature, the relative permittivity has shown to vary between 3.71 to 3.34 for a pre-stretch of 300% and 400%, as reported by Wissler and Mazza (2007). But, larger values have also been reported to range between 4.5 to 4.7 (Kofod et al., 2003). Our predictions fall closer to ones given by Wissler and Mazza (2007); however, they are lower by 11% to 16%. The uncertainty associated with both the dielectric constant and the hyperelastic coefficients needs to be further investigated to better understand these differences.

To provide more insight into the change in tension during pre-stretch, application of the field, and deformation due to aerodynamic loads based on VIC data, we plot the in-plane second Piola-Kirchhoff stress in the center of the membrane over the set of load steps applied to the model for each electric field. This stress provides insight into the change in tension as the field is applied. Figure 12 shows that the stress initially follows the curve describing bi-axial stretching previously shown in Figure 9(b) prior to application of a field. As the field is incremented to the electrostatic experimental condition (with zero transverse displacement), the in-plane tension is reduced. Finally, the last set of load step increments describe the in-plane stress as the transverse displacements increase due to aerodynamic loads. Minimal

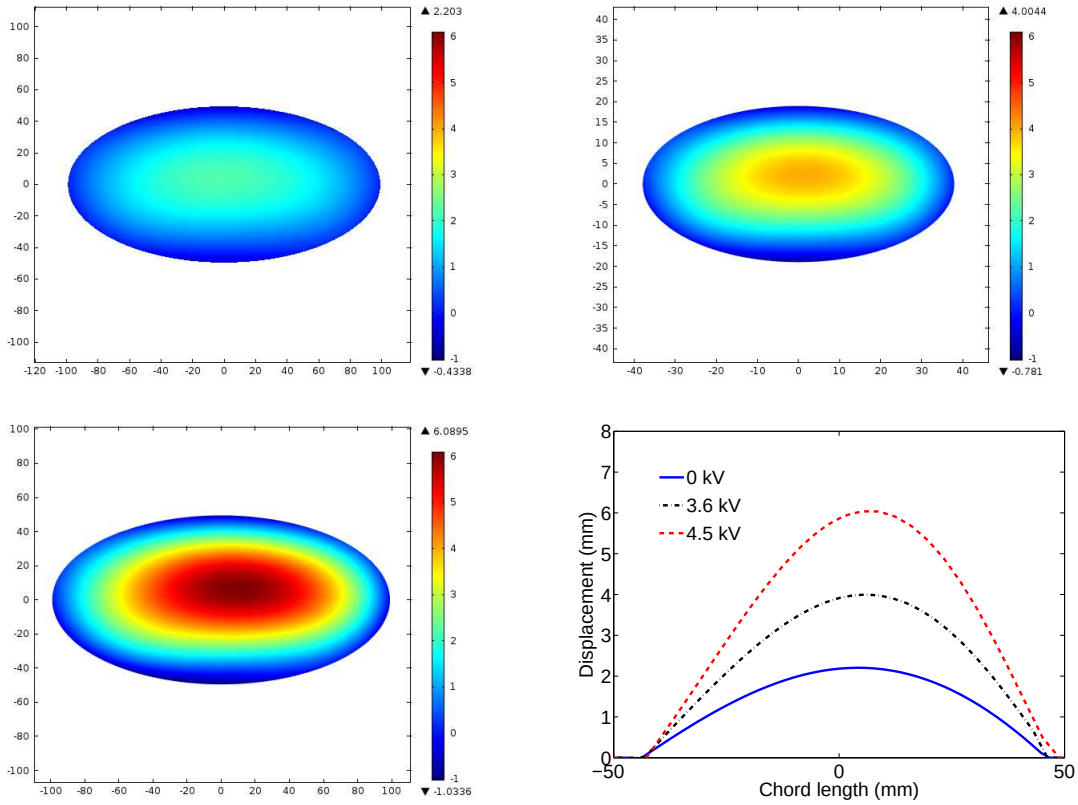

Figure 10: Finite element results of the membrane displacements (in mm) are illustrated for each voltage: (a) 0 kV, (b) 3.6 kV, and (c) 4.5 kV. In all these figures, the flow is moving from the top to bottom. In (d), a comparison of the displacements for each voltage is shown along the centerline of the wing along the chord direction. Note that the flow is moving from right to left.

changes in the tension are observed at the center point. It is important to note how the tension per unit length and the in-plane stresses change over the wing at the final deformation state for each voltage. Figures 13(a,c,e) illustrate the change in the in-plane Cauchy stress component (true stress, σ_{22}–chord direction) over the entire wing for the three different voltage cases. For 0 kV and 3.6 kV, the Cauchy stress is approximately constant; however, significant differences occur at the larger field of 4.5 kV. Similiar variations in magnitude of the Cauchy stress in the spanwise direction occur. Despite this difference, if the Cauchy stress is multiplied by the true thickness, the tension per unit length remains approximately constant even for the largest voltage case; see Figure 13(b,d,f).

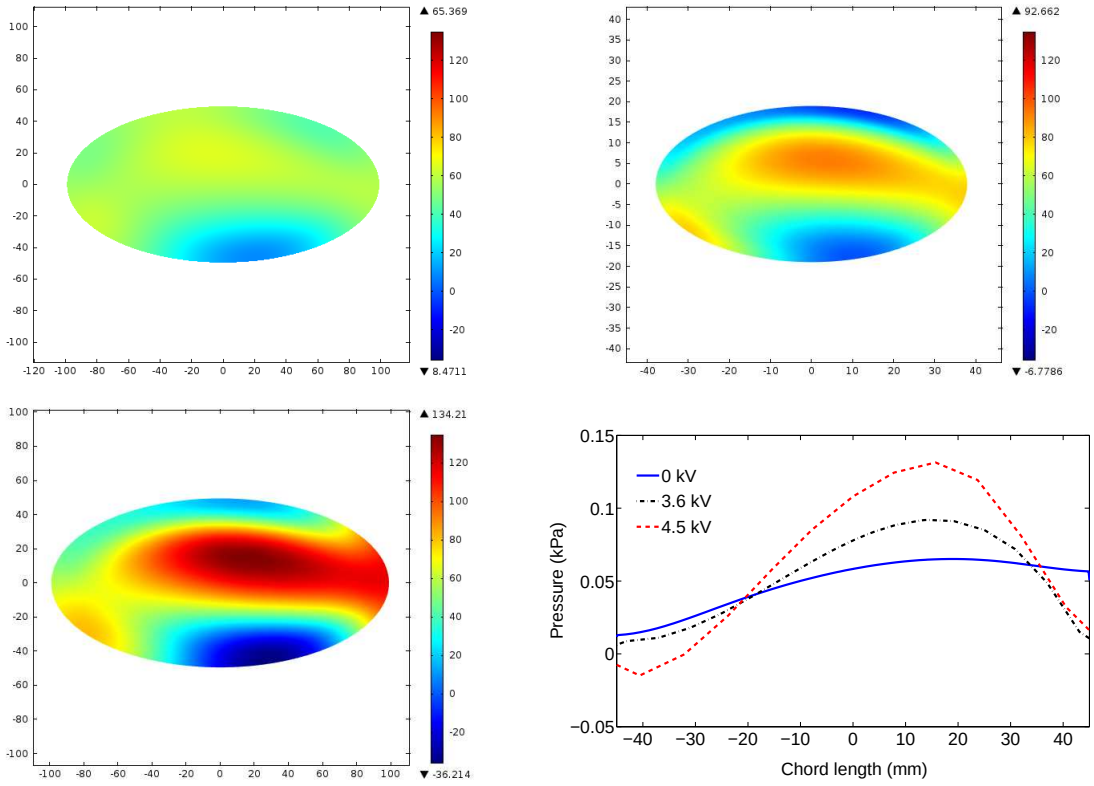

Figure 11: Finite element results of the pressure estimates are illustrated for each voltage: (a) 0 kV, (b) 3.6 kV, and (c) 4.5 kV. In figures (a-c), the flow is moving from top to bottom. In (d), a comparison of the pressure of each voltage is shown along the centerline of the wing along the chord direction. Note that the flow is moving from right to left.

4.2 Weber Number Correlations

Lastly, the results are compared to Weber number scaling relations similar to those given in Song et al. (2008). The Weber number is defined by the ratio of the aerodynamic normal force normalized by the modulus times the membrane thickness. Experimentally, the Weber number is defined by $We_{exp} = \frac{1}{2}\rho U^2 C_L c/(Et)$ where ρ is the density of air, U is the flow speed, c is a characteristic length of the membrane, E is the modulus and t is the membrane thickness. This definition of We is compared to analytical calculations based on the average finite element pressure which is averaged by integrating the pressure along the chordwise direction on the spanwise center of the wing. The analytic Weber number is $We_{an} = p_{avg}c/(Et)$ where p_{avg} is the average pressure. We take the characteristic length of the wing to be 10 mm and the

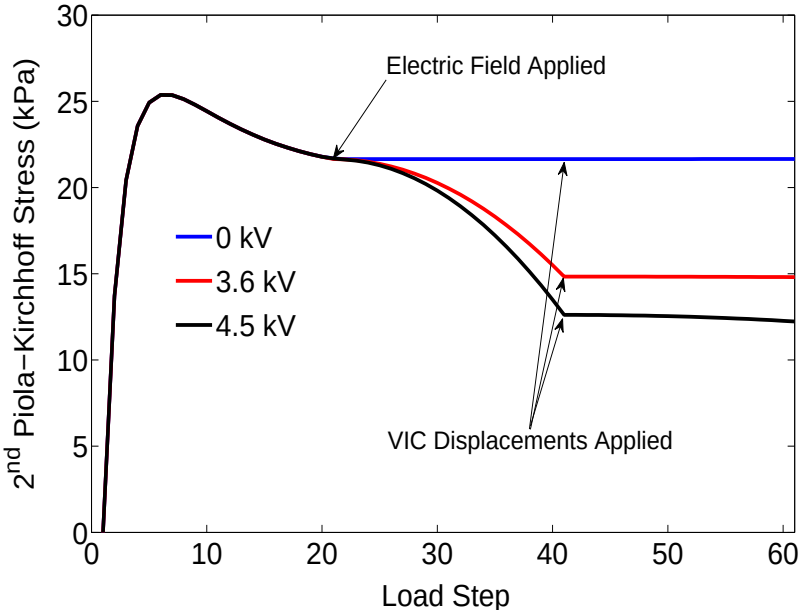

Figure 12: Plot of $\widetilde{T}_{22}$ versus load steps calculated in the finite element model. The results illustrate how in-plane stresses are reduced as the field is applied.

modulus is $E = 2(1+\nu)\mu$ where the Poisson ration is $\nu = 0.5$ and the effective modulus is $\mu = \sum_{p=1}^{3} \mu_p$ from Table 2. The results illustrate that We_{exp} and We_{an} are on the same order of magnitude for the cases simulated (Re_c=63k, 17° AoA). The error between the two cases ranges between 34% and 38%; see Table 3.

5 Concluding Remarks

An electroactive membrane has been experimentally characterized and modeled under different low Reynolds number flows. The presence of an electric field has shown to dramatically change the deformation of the membrane under aerodynamic loads where the maximum time-averaged displacement increased from 2 mm to 6 mm as the voltage increased from 0 V to 4.5 kV. For Re_c=63k, the coefficient of lift increased 20% as the voltage was increased from 0 kV to 4.5 kV and stall was delayed by approximately 5°. The aerodynamic efficiency (C_L/C_D) was found to be greatest at the intermediate 3.6 kV for Re_c=63k. For the lower

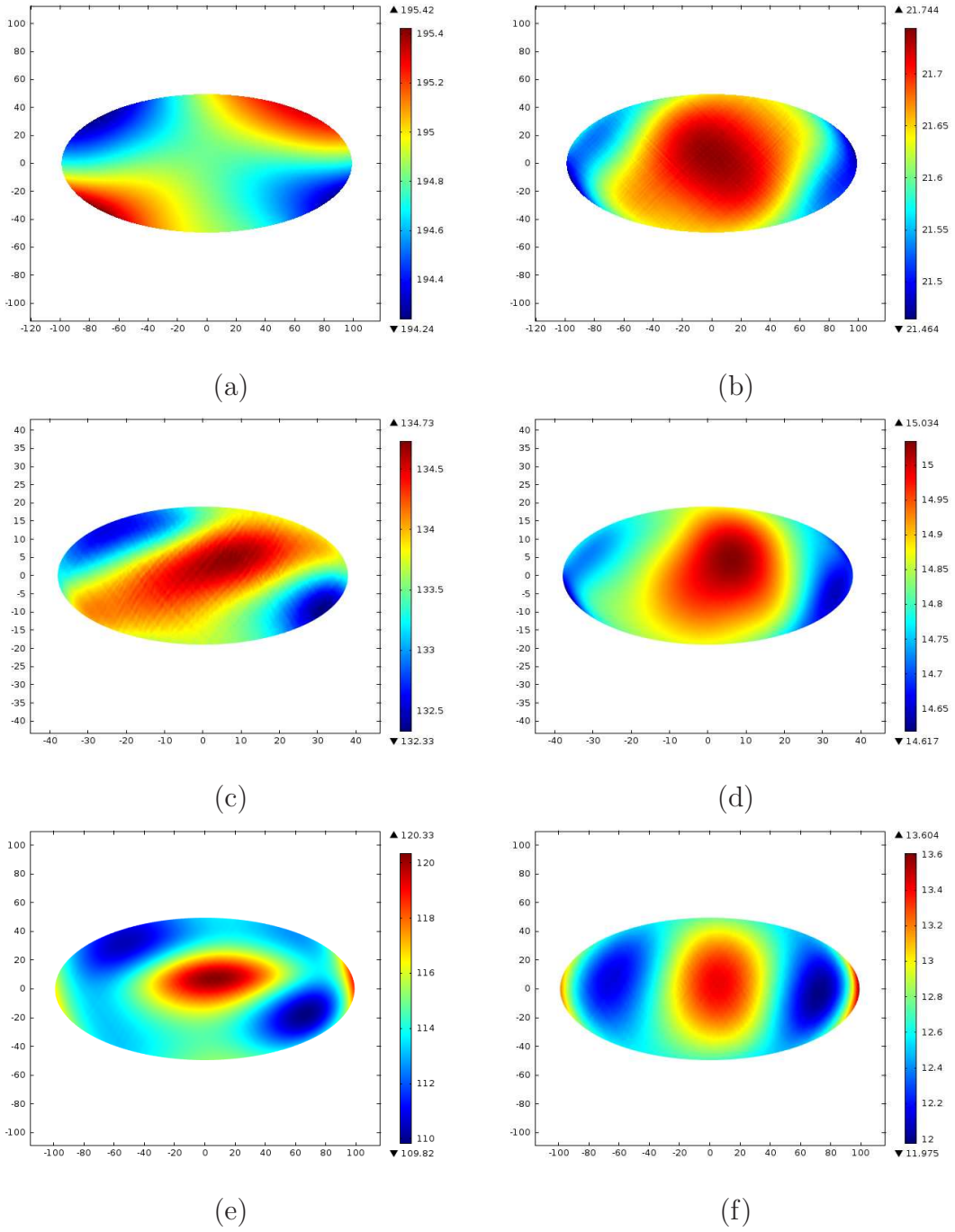

Figure 13: A comparison of the Cauchy stress component σ_{22} in (a,c,e) for 0 kV, 3.6 kV, and 4.5 kV with the corresponding tension per unit length in the x_2 direction in (b,d,f) for the respective voltages.

Reynolds number case, the lift increased as a function of voltage increase, but the aerodynamic efficiency was highest at 0 kV and monotonically decreases as the voltage increased. The re-

sults suggest that the pre-tension at 300% is ideal for the lower Reynolds number flow, but not for Re_c=63k. The results clearly illustrate that wing camber of an electroactive membrane can be controlled by an electric field.

To further analyze the results, a finite deformation membrane model was developed that couples the experimental VIC displacement data with the electro-mechanical membrane governing equations. The model reasonably matched VIC data by penalizing differences between the finite element nodal displacements and a polynomial fit to the VIC data. This methodology provides a numerical tool to quantify aerodynamic forces on the membrane surface as a function of the hyperelastic constitutive relations and electrostatic stresses based on dielectric behavior. Reasonable predictions of lift were achieved using a uni-axial hyperelastic model fit to experiments and isotropic dielectric coefficients given in the literature. Errors on the order of 6% to 16% were obtained where the uncertainty in model predictions increased as the voltage increased. Possible sources of this error include neglecting viscoelasticity and time-varying deformation coupled to turbulent flow around the membrane. Further, the VIC measurements were limited to a region that did not extend fully to the membrane edge. The pressure calculated over the VIC measurement region was extrapolated to be proportional over the entire wing area and neglected complex flow conditions along the wing boundary. These boundary conditions between the fluid and structure should be investigated further to improve predictions of aerodynamic loads across adaptive membrane wings.

6 Acknowledgments

The authors gratefully appreciate support through an ASEE Summer Faculty Fellowship Program, utilization of the REEF wind tunnel facilities, and partial support through AFOSR grant FA9550-09-1-0353 (Program Monitor: Dr. Douglas R. Smith). W. Oates also appreciates mentoring by Dr. Gregg Abate while working at Eglin AFRL and the REEF and uncertainty measurements provided by Adam Hart and Larry Ukeiley. This research was performed while U. Chakravarty held a National Research Council Research Associateship Award at the U.S.

Air Force Research Laboratory.

Appendix

The VIC data was fit to a polynomial using the Matlab function `fit` to facilitate comparison of the data directly within the finite element model. Fits to displacement were taken at each electric field case. The fifth order polynomial given below are scaled to the reference domain whereas the deformed configuration is based on a pre-stretch of $\lambda_0 = 3$.

$$\begin{aligned} u_3^{VIC} = {} & p_{00} + p_{10}X_1 + p_{01}X_2 + p_{20}X_1^2 + p_{11}X_1X_2 + p_{02}X_2^2 + p_{30}X_1^3 + p_{21}X_1^2X_2 + p_{12}X_1X_2^2 + \dots \\ & p_{03}X_2^3 + p_{40}X_1^4 + p_{31}X_1^3X_2 + p_{22}X_1^2X_2^2 + p_{13}X_1X_2^3 + p_{04}X_2^4 + p_{50}X_1^5 + p_{41}X_1^4X_2 + \dots \\ & p_{32}X_1^3X_2^2 + p_{23}X_1^2X_2^3 + p_{14}X_1X_2^4 + p_{05}X_2^5 \end{aligned} \tag{10}$$

References

Albertani, R., Babcock, J., 2008. Analysis of wind tunnel unsteady aerodynamic data of flexible micro air vehicle wings. In: 26th AIAA Applied Aerodynamics Conference.

Albertani, R., Khambatta, P., Hart, A., Ukeiley, L., Oyarzun, M., Cattafesta, L., Abate, G., et al., 2009. Validation of a low Reynolds number aerodynamic characterization facility. In: 47th AIAA Aerospace Sciences Meeting.

Bar-Cohen, Y., Zhang, Q., 2008. Electroactive polymer actuators and sensors. MRS Bulletin, 173–177.

Baur, J., Silverman, E., 2007. Challenges and opportunities in multifunctional nanocomposite structures for aerospace applications. MRS Bulletin 32, 328–334.

Bertotti, G., 1998. Hysteresis in Magnetism: for Physicists, Materials Scientists, and Engineers. Academic Press, San Diego, CA.

Bin, J., Uzun, A., Hussaini, M., 2011. Adaptive mesh redistribution method for domains with complex boundaries. J. Comput. Phys. 230, 3178–3204.

Boyd, J., Lagoudas, D., 1996. A thermodynamical constitutive model for shape memory materials. Part II. The sma composite material. Int. J. Plasticity 12 (7), 843–873.

Bustamante, R., Dorfmann, A., Ogden, R., 2009. Nonlinear electroelastostatics: A variational framework. Z. angew. Math. Phys. 60, 154–177.

Cottet, G.-H., Maitre, E., Milcent, T., 2008. Eulerian formulation and level set models for incompressible fluid-structure interaction. ESAIM: Mathematical modeling and numerical analysis 42, 471–492.

Dunne, T., Rannacher, R., 2006. Adaptive finite element simulation of fluid-structure interaction based on an Eulerian variational formulation. Springer (H.-J. Bungartz and M. Schafer, ed.), Berlin, Germany.

Fox, J., Goulbourne, N., 2009. Electric field-induced surface transformations and experimental dynamic characterization of dielectric elastomer membranes. J. Mech. Phys. Solids 55, 1417–1435.

Gordnier, R., 2009. High fidelity computational simulation of a membrane wing airfoil. J. Fluids Struct. 25, 897–917.

Holzapfel, G., 2000. Nonlinear Solid Mechanics. John Wiley & Sons, Inc., Chichester.

Huang, M., Brinson, L., 1998. A multivariant model for single crystal shape memory alloy behavior. J. Mech. Phys. Solids 46 (8), 1379–1409.

Jaffe, B., Cook, W., Jaffe, H., 1971. Piezoelectric Ceramics. Academic Press, London.

Kittel, C., 1949. Physical theory of ferromagnetic domains. Rev. Mod. Physics 21 (4), 541–583.

Kofod, G., Sommer-Larsen, P., 2005. Silicone dielectric elastomer actuators: Finite-elasticity model of actuation. Sensors and Actuators A 122, 273–283.

Kofod, G., Sommer-Larsen, P., Kornbluh, R., Pelrine, R., 2003. Actuation response of polyacrylate dielectric elastomers. J. Int. Mater. Syst. Struct. 14, 787–793.

Lines, M., Glass, A., 1977. Principles and Applications of Ferroelectrics and Related Materials. Clarendon Press, Oxford.

Liu, Y., Gall, K., Dunn, M., Greenberg, A., Diani, J., 2006. Thermomechanics of shape memory polymers: Uniaxial experiments and constitutive modeling. Int. J. Plasticity 22 (2), 279–313.

McMeeking, R., Landis, C., 2005. Electrostatic forces and stored energy for deformable dielectric materials. J. Appl. Mech 72, 581–590.

Molki, M., Breuer, K., 2010. Oscillatory motions of a prestrained compliant membrane caused by fluid-membrane interaction. J. Fluids Struct. 26, 339–358.

Newton, J., Morton, J., Clark, J., Oates, W., 2012. Modeling and characterization of stiffness controlled robotic legs using dielectric elastomers. SPIE Smart Materials and Structures Conference, San Diego, CA 8340, 83400Z.

Plante, J., Dubowsky, S., 2006. Large-scale failure modes of dielectric elastomer actuators. Int. J. Solids Struct. 43, 7727–7751.

Rojratsirikul, P., Wang, Z., Gursul, I., 2010. Effect of pre-strain and excess length on unsteady fluid-structure interactions of membrane airfoils. J. Fluids Struct. 26, 359–376.

Schweizerhof, K., Ramm, E., 1984. Displacement dependent pressure loads in nonlinear finite element analysis. Computers and Structures 18 (6), 1099–1114.

Song, A., Tian, X., Israili, E., Galvao, R., Bishop, K., Swartz, S., Breuer, K., 2008. Aeromechanics of membrane wings with implications for animal flight. AIAA J. 46 (8), 2096–2106.

Warner, M., Terentjev, E., 2007. Liquid Crystal Elastomers–Revised Edition. Oxford Science Publications, Oxford.

Wissler, M., Mazza, E., 2005. Modeling of a pre-strained circular actuator made of dielectric elastomers. Sensors and Actuators A 120, 184–192.

Wissler, M., Mazza, E., 2007. Electromechanical coupling in dielectric elastomer actuators. Sensors and Actuators A: Physical 138 (2), 384 – 393.
URL http://www.sciencedirect.com/science/article/pii/S0924424707004335

Zhao, X., Hong, W., Suo, Z., 2007. Electromechanical hysteresis and coexistent states in dielectric elastomers. Phys. Rev. B 76, 134113–1–134113–9.

Table 1: Maximum standard deviation ($\sigma[\cdot]$) of the strains $\Delta\bar{\epsilon}_{xx}$, $\Delta\bar{\epsilon}_{yy}$, and $\Delta\bar{\epsilon}_{xy}$ for voltages 0 V, 3.6 kV and 4.5 kV and flight speeds 6 m/s and 10 m/s

	$\sim\max(\sigma[\epsilon_{xx}])$	
Voltage (kV)	6 m/s	10 m/s
0	10^{-4}	10^{-4}
3.6	10^{-4}	10^{-4}
4.5	10^{-4}	10^{-3}
	$\sim\max(\sigma[\epsilon_{yy}])$	
Voltage(kV)	6 m/s	10 m/s
0	10^{-3}	10^{-3}
3.6	10^{-3}	10^{-3}
4.5	10^{-3}	10^{-3}
	$\sim\max(\sigma[\epsilon_{xy}])$	
Voltage(kV)	6 m/s	10 m/s
0	10^{-4}	10^{-3}
3.6	10^{-4}	10^{-3}
4.5	10^{-4}	10^{-3}

Table 2: A summary of the hyperelastic material parameters introduced in the membrane finite element model. The uniaxial model parameters correspond to the model predictions fit to uniaxial data described elsewhere Newton et al. (2012). The shear moduli (μ_i) are given in kPa and the constants (α_i) are unitless.

	μ_1	μ_2	μ_3	α_1	α_2	α_3
uniaxial model fit	16.8	7.96	2.63×10^{-3}	0.30	1.01	2.63

Table 3: A summary of Weber number calculations comparing the experimental ($We_{exp} = \frac{1}{2}\rho U^2 C_L c/(Et)$) and the analytical ($We_{an} = p_{avg} c/(Et)$).

	0 kV	3.6 kV	4.5 kV
We_{exp}	0.72	0.75	0.91
We_{an}	1.11	1.21	1.48

Table 4: Polynomial coefficients used in fitting the VIC transverse displacement data for finite element model comparisons.

Coefficients	0 kV	3.6 kV	4.5 kV
p_{00}	2.18	3.91	5.86
p_{10}	-2.47×10^{-3}	7.73×10^{-3}	3.38×10^{-2}
p_{01}	3.03×10^{-2}	8.53×10^{-2}	1.60×10^{-1}
p_{20}	-1.47×10^{-3}	-3.08×10^{-3}	-4.70×10^{-3}
p_{11}	2.32×10^{-3}	8.46×10^{-4}	2.21×10^{-3}
p_{02}	-1.06×10^{-2}	-2.04×10^{-2}	-3.28×10^{-2}
p_{30}	8.23×10^{-6}	2.36×10^{-6}	-1.81×10^{-5}
p_{21}	-7.83×10^{-5}	-1.91×10^{-4}	-2.89×10^{-4}
p_{12}	-1.70×10^{-5}	-9.96×10^{-5}	-3.37×10^{-4}
p_{03}	-1.14×10^{-4}	-4.35×10^{-4}	-8.59×10^{-4}
p_{40}	-4.30×10^{-7}	-4.45×10^{-7}	-7.36×10^{-7}
p_{31}	-2.87×10^{-7}	-8.83×10^{-7}	-2.19×10^{-6}
p_{22}	2.77×10^{-6}	7.03×10^{-6}	1.09×10^{-5}
p_{13}	-9.51×10^{-7}	-3.53×10^{-6}	-1.04×10^{-5}
p_{04}	3.97×10^{-6}	1.48×10^{-5}	3.19×10^{-5}
p_{50}	-5.19×10^{-9}	-9.33×10^{-9}	-1.44×10^{-8}
p_{41}	6.57×10^{-8}	1.43×10^{-7}	1.82×10^{-7}
p_{32}	1.85×10^{-8}	4.96×10^{-8}	1.66×10^{-7}
p_{23}	1.27×10^{-7}	5.35×10^{-7}	8.07×10^{-7}
p_{14}	1.71×10^{-7}	3.69×10^{-7}	9.59×10^{-7}
p_{05}	2.85×10^{-8}	6.31×10^{-7}	1.23×10^{-6}